Supercoiling Enhances DNA Mobility by Reducing Threadings and Entanglements

Jan Smrek[1] and Davide Michieletto[2, 3]

[1] *Faculty of Physics, University of Vienna, Boltzmanngasse 5, A-1090 Vienna, Austria*
[2] *School of Physics and Astronomy, University of Edinburgh, Peter Guthrie Tait Road, Edinburgh, EH9 3FD, UK*
[3] *MRC Human Genetics Unit, Institute of Genetics and Molecular Medicine, University of Edinburgh, Edinburgh EH4 2XU, UK*

DNA is increasingly employed for bio and nanotechnology thanks to its exquisite versatility and designability. Most of its use is limited to linearised and torsionally relaxed DNA but non-trivial architectures and torsionally constrained – or supercoiled – DNA plasmids are largely neglected; this is partly due to the limited understanding of how supercoiling affects the rheology of entangled DNA. To address this open question we perform large scale Molecular Dynamics (MD) simulations of entangled solutions of DNA plasmids modelled as twistable chains. We discover that, contrarily to what generally assumed in the literature, larger supercoiling increases the average size of plasmids in the entangled regime. At the same time, we discover that this is accompanied by an unexpected increase of diffusivity. We explain our findings as due to a decrease in inter-plasmids threadings and entanglements.

The deoxyribonucleic acid (DNA) is not only the central molecule of life but it is now increasingly employed for bio-compatible and responsive materials – such as DNA hydrogels [1] and origami [2] – with applications in medicine and nanotechnology [3]. One feature that renders DNA a unique polymer is its ability to encode information, and this is now extensively leveraged to make complex structures [3–5] and even self-replicating materials [6]; another feature that distinguishes DNA from other synthetic polymers is its unique geometry, i.e. that of a (right-handed) helix with a well-defined pitch, which entails that DNA can display both bending and torsional stiffness [7]. Oppositely to the information-encoding feature of DNA, its geometrical features are far less exploited to create synthetic materials. In fact, DNA is at present largely employed in its simplest geometrical form, i.e. that of a linear or nicked circular (torsionally unconstrained) molecule [8–12]. In spite of this, most of the naturally occurring DNA is under torsional and topological constraints, either because circular and non-nicked (as in bacteria) or because of the binding of proteins that restrict the relative rotation of base-pairs in eukaryotes [13–16]. The torsional stress stored in a closed DNA molecule cannot be relaxed but only re-arranged or converted into bending in order to minimise the overall conformational free energy [17–19]. This entails that supercoiling – the linking deficit between sister DNA strands with respect to their relaxed state – can potentially carry conformational information [20] which can even regulate gene transcription [21]. Here, we propose that supercoiling may also be leveraged to tune the dynamics of DNA plasmids in solution, thus potentially allow for a fine control over the rheology of DNA-based complex fluids in a way that is orthogonal to varying DNA length [22], concentration [23] or architecture [9, 24].

Entangled solutions of DNA plasmids are not only interesting because of potential applications in bio and nanotechnology but also because they are a proxy to study fundamental questions on the physics of ring polymers [9, 25, 26]. To characterise the effect of DNA supercoiling in entangled solutions, here we perform large scale Molecular Dynamics simulations of entangled DNA plasmids (Fig. 1A-C), modelled as coarse-grained twistable chains [27]. We discover that while isolated DNA plasmids typically display a collapse with increasing levels of supercoiling (estimated via simulations [28] or gel electrophoresis [29]), here we show that entangled DNA plasmids typically increase their average size for increasing values of supercoiling. Importantly, we further discover that in spite of this, larger supercoiling is accompanied by an *enhanced* mobility of the plasmids. This finding is counter-intuitive and in marked contrast with standard polymer systems [30] whereby larger polymer sizes correlate with slower diffusion. Finally, we quantify the abundance of threadings and entanglements and discover that larger supercoiling decreases both these topological constraints, hence explaining the enhanced mobility. Given the lack of detailed studies on the dynamics of entangled supercoiled plasmids and their current technical feasibility [31], we argue that achieving a better understanding of these systems will not only suggest new strategies to realise the next-generation of biomimetic DNA-based materials but also shed light into the dynamics of DNA *in vivo*.

RESULTS AND DISCUSSION

Model

DNA is represented as a twistable elastic chain [27, 32] made of beads of size $\sigma_b = 2.5$ nm$= 7.35$ bp connected by finitely-extensible springs and interacting via a purely repulsive Lennard-Jones potential to avoid spontaneous chain-crossing [33]. In addition to these potentials, a

bending stiffness of $l_p = 50$ nm [7] is set via a Kratky-Porod term and two torsional springs (dihedrals) constrain the relative rotation of consecutive beads, ψ, at a user-defined value ψ_0. The torsional angle between consecutive beads ψ is determined by decorating each bead with three patches which provides a reference frame running along the DNA backbone. We finally impose a stiff harmonic spring to constrain the tilt angle $\theta = \pi$ so to align the frame with the backbone, i.e. along its local tangent (see Fig. 1D). The simulations are performed at fixed monomer density $\rho\sigma_b^3 = 0.08$ and by evolving the equation of motion for the beads coupled to a heat bath in LAMMPS [34] (see Methods).

The user-defined angle ψ_0 directly determines the thermodynamically preferred pitch of the twisted ribbon as $p = 2\pi/\psi_0$ and, in turn, this fixes the preferred linking number to $Lk = M/p$, where M is the number of beads in the plasmid. The twist is enforced by a harmonic potential with stiffness $\kappa_t = 50\sigma_b = 125$ nm comparable with the torsional persistence length of DNA. In this model, the relaxed linking number is $Lk_0 = 0$ and so the degree of supercoiling $\sigma \equiv \Delta Lk/M = Lk/M = 1/p$. This is set by initialising the patchy-polymer as a flat ribbon and by subsequently imposing the angle ψ_0 in order to achieve the desired σ (which may be zero, if $\psi_0 = 0$ or $p = \infty$). It should be noted that we also will consider relaxed plasmids in which the torsional stiffness is set to $\kappa_t = 0$ mimicking fully nicked plasmids. Finally, it should be recalled that for non-nicked circular DNA, the exchange of local torsion (twist Tw) into bending (writhe Wr) must obey the White-Fuller-Călugăreanu (WFC) [35–37] theorem, i.e. $Lk = Tw + Wr$, thus conserving the linking number Lk (and thus the supercoiling $\sigma = \Delta Lk/M$) between the two DNA single strands (Fig. 1B-D). Notice that our polymer model is symmetric with respect to supercoiling and therefore we will refer to σ without specifying the sign.

Supercoiling Increases the Average Size of DNA Plasmids in Entangled Conditions

The conformational properties of polymers in solution are typically studied in terms of the gyration tensor

$$R_T^{\alpha\beta} = \frac{1}{2M^2} \sum_{i,j=1}^{M} \left(r_i^\alpha - r_j^\alpha\right)\left(r_i^\beta - r_j^\beta\right) \qquad (1)$$

where r_i^α denotes the coordinate α of the position of bead i. The (square) radius of gyration is then defined as the trace, $R_g^2 \equiv \mathrm{Tr}[\mathrm{R_T}]$. Interestingly, we find that the time and ensemble average of R_g^2 scales as $\langle R_g^2 \rangle \sim L^{2\nu}$, with the metric exponent $\nu = 1/2$ and $\nu = 3/5$ for relaxed and highly supercoiled plasmids, respectively (for $M \geq 200$, see Fig. 2A and Fig. S1 in SI). These two regimes are compatible with the ones for ideal ($\nu = 1/2$) and self-avoiding ($\nu \simeq 0.588$) random walks; this finding suggests that relaxed plasmids in entangled solutions ($\nu = 1/2$) assume conformations similar to the ones of standard flexible, albeit short, ring polymers [38]. At the same time, for larger values of σ, the self-interactions driven by writhing (see Fig. 1B,C) are no longer screened by the neighbours and we thus observe a larger metric exponent ν compatible with a self-avoiding walk.

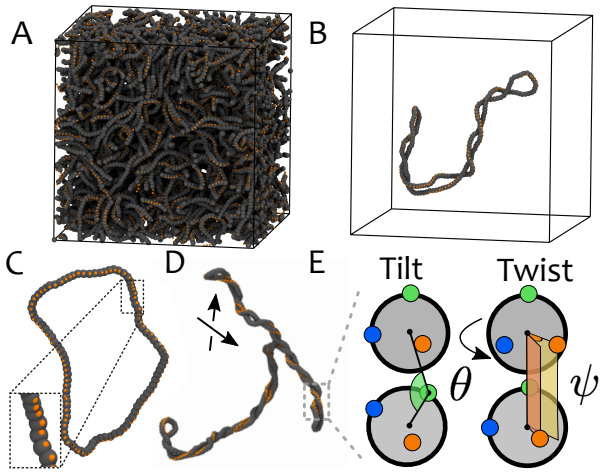

Figure 1. **A** Snapshot of simulation of entangled plasmids with length $L = 200\sigma_b \simeq 1.47kbp \simeq 0.5\mu m$ and $\sigma = 0.04$. **B** A single plasmid taken from **A**. **C,D** Snapshots of other plasmids in solutions with (**C**) $\sigma = 0$, $L = 0.25\mu m$ and (**D**) $\sigma = -0.06$, $L \simeq 1\mu m$. Backbone beads are shown in grey, one set of patches are shown in orange. The other patches are not shown for clarity. **E** Sketch of tilt θ and tilt ψ_1 between consecutive beads (an equivalent ψ_2 is set between blue patches, not shown). The tilt angle θ is subject to a stiff potential with equilibrium $\theta_0 = 0$ to maintain the frame co-planar and aligned with the backbone.

The effect of supercoiling on the average size of plasmids can be better appreciated in Fig. 2B where we show the (squared) radius of gyration rescaled by its value for relaxed plasmids and plotted against supercoiling. One can readily notice that, importantly, for long plasmids (e.g. $M \geq 400 \simeq 3$ kb) the greater the supercoiling the *monotonically* larger their typical size. We highlight that this behaviour is highly counter-intuitive as one expects that supercoiling induces the compaction of a polymer. For instance, supercoiled plasmids travel faster than their relaxed counterparts in gel electrophoresis [29]. Additionally, supercoiling is often associated with the packaging of the bacterial genome [39, 40] and with organisation into topological domains in eukaryotes [14, 41, 42]. Interestingly, the observed monotonic increase of R_g with supercoiling is in marked contrast with the overall shrinking seen in dilute conditions [28] (which is also reproduced by our model in dilute conditions, see Fig. S1 in SI). We argue that this stark difference is due to inter-chain effects as it is mostly evident for long chains but remarkably absent for short ones (Fig. 2B).

For short plasmids ($M = 100 \simeq 730bp$) we observe an interesting exception to the behaviour described above

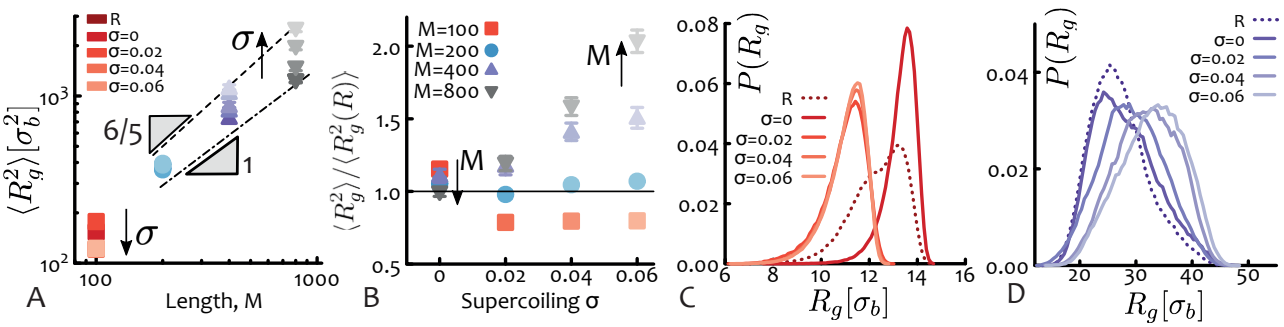

Figure 2. **Supercoiling Increases Plasmids Size in Entangled Conditions. A-B** Radius of gyrations R_g plotted against (**A**) contour length M and (**B**) supercoiling σ. Notice that for short lengths $M = 100$, increasing σ induces a collapse of the plasmids whereas for longer lengths it drives swelling. The scaling of R_g as a function of plasmid length is compatible with those of ideal and self-avoiding walks for relaxed and highly supercoiled plasmids, respectively. **C** The distribution of R_g for $M = 100$ is weakly bimodal showing that plasmids can be in either an "open" or a "collapsed" state. Setting a supercoiling $\sigma = 0$ stabilises the open state whereas $\sigma > 0$ induces writhing and collapse. **D** For longer plasmids ($M = 400$) larger supercoiling σ broadens the distribution and drives enlarges the average size. The unit of length is $\sigma_b = 2.5$ nm.

whereby the typical size is non-monotonic for increasing supercoiling levels. More specifically, for $\sigma = 0$ we find that the conformations are typically larger than the relaxed ones, but they suddenly become more collapsed for $\sigma > 0$ (Fig. 2B). To investigate this behaviour further we examined the distributions of radius of gyration and noticed that relaxed short plasmids display a weakly bimodal distribution that is not found in larger plasmids (Fig. 2C,D). This bimodal distribution reflects the fact that short relaxed plasmids can be found in two typical conformation states: either open (large R_g) or more collapsed (small R_g). The switching between these two typical conformations is instead forbidden when a certain supercoiling is imposed as all allowed conformations must satisfy the WFC topological conservation law. More specifically, zero supercoiling ($\sigma = 0$) hinders the writhing of the plasmid and, given their short length ($L/l_p = 5$), it would be energetically too costly to writhe multiple times with opposite sign to achieve a null global writhe. This entails that short plasmids are locked into open, not self-entangled conformations. On the contrary, for $\sigma > 0$, the imposed writhing induces a conformational collapse, akin to a sharp buckling transition [43].

We note that the stable open state at $\sigma = 0$ for short plasmids is akin to the one computationally observed in dense solutions of semiflexible rings [44]. These systems are expected to give rise to exotic columnar phases which would be thus intriguing to investigate in the context of dense solutions of short null-supercoiled plasmids.

We finally stress once more that the monotonic increase observed for long plasmids of their typical size with supercoiling is neither expected nor trivial and is in marked contrast with the overall shrinking behaviour found in the literature for long dilute supercoiled plasmids [28]. Since the monomer concentration is constant for all the system studied, one would naïvely expect that the effective c/c^* is larger (the critical entanglement concentration scales as $c^* \sim M/R_g^3$). In turn, this implies more inter-chain entanglements which add up to the already more numerous intra-chain entanglements due to the increase of self-crossings (writhing). As a consequence, we also expect highly supercoiled long plasmids to have reduced mobility with respect to their relaxed counterparts. In summary, based on the results in Fig. 2 and simple arguments, we expect that supercoiling hinders the diffusion of plasmids.

Supercoiling Enhances DNA Mobility

We study the dynamics of the entangled plasmids at different levels of supercoiling by computing the time- and ensemble-averaged mean squared displacement (TAMSD) of the centre of mass (CM) of the plasmids as $g_3(t) = \langle \boldsymbol{r}_{CM,i}(t+t_0) - \boldsymbol{r}_{CM,i}(t_0)\rangle_{i,t_0}$ (other g_i quantities are reported in Fig. S4 in SI). Curves for g_3 are shown in Fig. 3A,B for different values of plasmid supercoiling and length. Strikingly, we find that higher values of σ yield faster mobility especially for longer plasmids. We recall that this is at first unexpected given the monotonically larger size discussed in the previous section.

The diffusion coefficient of the centre of mass computed as $D_{CM} = \lim_{t\to\infty} g_3(t)/6t$ allows us to more precisely quantify how the mobility of the plasmids changes as a function of length and supercoiling. In particular, we find that while D_{CM} attains a plateau at small σ, at larger supercoiling it increases exponentially (see Fig. 3C) albeit more simulations are needed to confirm this conjecture (see below for an argument supporting the exponentially faster mobility). Additionally, we find that the diffusion coefficient as a function of plasmid length scales as $D_{CM} \sim M^{-2.5}$, compatible with the scaling of flexible and much longer ring polymers [45] (Fig. 3D). [Note that the solutions with $M = 800$ are not displaying a freely diffusive behaviour in spite of the fact that we ran them for more than 10^7 Brownian times (see Tab. S1 in SI);

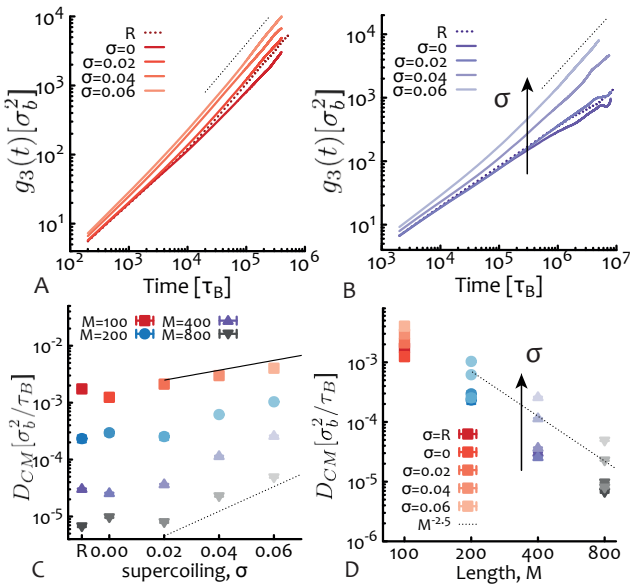

Figure 3. **Supercoiling Enhances Plasmid Mobility. A-B** TAMSD of the plasmids for (**A**) $M = 100 \simeq 730$ bp) and (**B**) $M = 400 \simeq 3$ kbp). Dashed lines are linear functions of lagtime as a guide for the eye. **C-D** Diffusion coefficient of the centre of mass $D_{CM} = \lim_{t\to\infty} g_3(t)/6t$ against (**C**) supercoiling σ and (**D**) length M. In **C** exponentials $\sim \exp(\sigma/0.05)$ (solid) and $\sim \exp(\sigma/0.02)$ (dashed) are drawn as guide for the eye. In **D** a power law $\sim M^{-2.5}$ is fitted through the data for $\sigma = 0.04$. Error bars are comparable to symbol size. R = "relaxed".

in turn, D_{CM} is overestimated as its calculation assumes free diffusion. In spite of this, values of D_{CM} for $M = 800$ nicely follow the general trend of the other datasets (see Fig. 3C,D).]

It should be highlighted that the agreement of the dynamical exponent found here with the one for longer and more flexible rings is unexpected, as for shorter ring polymers (smaller L/l_p and comparable with the rings studied here) the dynamical exponent was shown to be smaller (about 1.5 [45]). We speculate that this more severe dependence on plasmid length may be due to the fact that DNA has a large persistence length ($l_p = 20\sigma_b \simeq 50$ nm) which can thus reduce the effective entanglement length [46]. In agreement with this argument, entangled solutions of semi-flexible and stiff ring polymers vitrify in certain concentration regimes [47] implying that large stiffness may exacerbate topological constraints. In particular, the observed jamming was conjectured to be related to threading [48–51], allowed by the swelling of the rings' conformations [47]. Motivated by this relationship between ring conformation and dynamics we now investigate in more detail the conformation properties of plasmids using shape descriptors derived from the gyration tensor.

Supercoiling Induces a Buckling Transition in Short Plasmids

The consequence of writhing on the plasmids conformations is not captured by R_g alone [52, 53]. Instead, it is informative to study shape descriptors which can be computed via the eigenvalues of the gyration tensor R_T (which we denote as a, b, c, with $a > b > c$ and $R_g^2 = a + b + c$). Typical shape descriptors are the asphericity [52–54] $a = ((a-b)^2 + (a-c)^2 + (b-c)^2)/2R_g^4$ which quantifies the deviation from a perfectly spherical arrangement and the nature of asphericity quantified by either the prolateness (see Fig. S2 in SI) or the anisotropy $an = 3(a^2 + b^2 + c^2)/(2R_g^4) - 1/2$ (shown in Fig. 4A,B). These shape descriptors reveal that for $M = 100$ and $\sigma = 0$, plasmids are stabilised in an open, highly symmetric and oblate (M&M's) state. Furthermore, they reveal that these short plasmids undergo a buckling transition to a closed, asymmetric and prolate (rugby ball) shape for $\sigma > 0$. The sharp first-order-like buckling transition (see Fig. 4A and SI) is weakened for larger contour lengths (see Fig. 4B), as self-writhing is energetically allowed even for $\sigma = 0$ (negative and positive self-crossings must cancel each other to satisfy the WFC conservation law). At the same time, both short and long plasmids display a general increase in asphericity, prolateness and anisotropy with increasing supercoiling, strongly suggesting that the plasmids assume elongated and double-folded conformations (see Fig. S2 in SI).

Supercoiling Decreases the Spanning Minimal Surface

It is natural to associate the open oblate and closed prolate conformations assumed by DNA plasmids to a larger and a smaller (minimal) area spanned by the contour, respectively [55]. The size of this area may be relevant for the dynamics because it could be "threaded" by neighbouring plasmids hence hindering the dynamics [48, 50, 56]. To quantify this in more detail we calculated the minimal surface using the algorithm used in Ref. [50, 55, 57] for relaxed ring polymers. We found that the minimal area grows linearly with the plasmids' contour, as expected [50] (Fig. 4C). Importantly, we also observed that it overall decreased with supercoiling with the notable exception of short $M \leq 200$ plasmids, for which there is a small increase for $\sigma = 0$ with respect to the relaxed case, again confirming the topological locking in open conformations (Fig. 2A).

A crude way to estimate the decrease in "threadable" area of a plasmid is via recursive bisections of a perfect circle into several connected smaller circles joined at a vertex mimicking writhe-induced self-crossing. Each times a circle is split into two smaller ones the new radii are $R' \simeq R/2$ and thus n circles (with $n-1$ self-crossings)

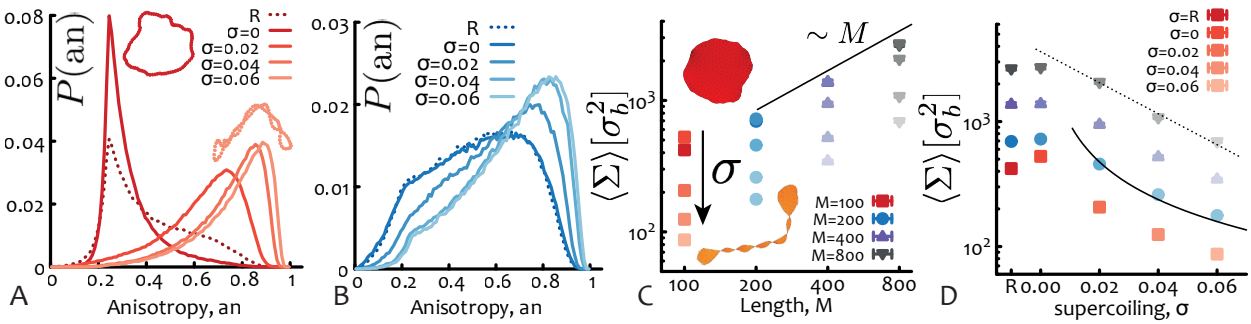

Figure 4. **Supercoiling Induces Buckling in Short Plasmids and Reduces the Threadable Area. A** The anisotropy shape descriptor (an, see text) for short plasmids $M = 100$ displays a sharp buckling transition between an open and roughly symmetric state for $\sigma = 0$ and a collapsed and anisotropic one for $\sigma > 0$. In inset, two examples of conformations are shown. **B** For longer plasmids ($M = 200$) supercoiling shifts the anistropy to larger values indicating a smoother transition to more prolate conformations. **C** Scaling of the average minimal surface size $\langle\Sigma\rangle$ as a function of plasmids length (solid line shows the linear scaling). In inset, two examples of surfaces for $M = 100$ are shown. **D** The size of the minimal surface area is monotonically decreased by supercoiling (with the exception of short $M \leq 200$ plasmids). The solid and dashed lines scale as $1/\sigma$ and $e^{-\sigma/0.035}$, respectively, and are drawn as a guide for the eye. R stands for "relaxed". The unit of length is $\sigma_b = 2.5$ nm. The error bars, typically smaller than the symbol size represent the error of the mean area.

have radii $R' = R/n$ yielding an overall spanning surface $\simeq n\pi(R/n)^2 \sim 1/n \sim 1/\sigma$. This crude estimation is in good agreement with the behaviour of the minimal surface albeit we cannot rule out other functional forms (for instance exponential, see Fig. 4D). [Note that the so-called magnetic moment and radius [58] give similar results albeit different scaling (see Fig. S3 in SI)].

Supercoiling Reduces Threadings

Motivated by the observation that the minimal surface – or "threadable area" – decreases with supercoiling, we decided to more precisely quantify the number of threadings per plasmid for different levels of supercoiling. To this end we identify a plasmid to be "passively threaded" by another when the minimal surface of the former is intersected by the contour of the latter (at least twice, as they are topologically unlinked) [50] (Fig. 5A). As shown in Fig. 5B, the average number of threadings per plasmid $\langle n_t \rangle$ appears to decrease exponentially with supercoiling and to mirror the behaviour of $\langle\Sigma\rangle$. [As for the minimal surface, a notable exception to this general trend is the case of short plasmids ($M = 100$) for which we find that $\langle n_t \rangle$ is statistically larger for $\sigma = 0$ than for relaxed plasmids.]

Based on these findings, we can also advance an argument as for why the mobility of the plasmids should increase with supercoiling: it was recently found that the dynamics of polymeric systems populated by threading topological constraints – for instance melts of tadpole-shaped polymers [24, 59] or compressed long plasmids [25] – slows down exponentially (with the number of threadings [24]). As seen in this section, increasing supercoiling reduces the threadable area and, in turn, the actual number of threadings; we thus expect the dynamics of highly supercoiled (threading-poor) plasmids to be exponentially faster than their relaxed (threading-rich) counterparts as seen in Fig. 3C. In spite of this our results are not definitive, and more work ought to be done.

Supercoiling Reduces Entanglements

The shape descriptors studied above suggest that the plasmids assume prolate double-folded conformations but it remains unclear whether the conformations are simply plectonemic (linear-like) or more branched into comb, star or tree-like structures [60]. We thus computed the local absolute writhe along the contour length, $W(s)$, from which the number and location of plectonemic tips can be extracted as the maxima of this function [61, 62] (see Methods). This calculation reveals that most of the conformations for $\sigma \geq 0.04$ have 2 tips consistent with [62], i.e. they mainly assume linear-like plectonemic conformations for the lengths considered in this work (see Fig. S5 in SI). [For smaller supercoiling it cannot unambiguously distinguish tips from other regions of large curvature.]

In light of this finding another apparent controversy arises. Indeed, arguably, linear chains of half the length as their ring counterparts diffuse slower than the rings due to reptation relaxation induced by ordinary entanglements of linear chains [45]; instead, we observe the opposite trend. To explain this we adapted the primitive path analysis (PPA) method [63] (see Fig. 5C,D and Methods) and determined an effective entanglement length N_e for highly supercoiled plasmids leveraging the fact that the tips of linear-like or branched conformations represent effective termini that can be pinned down. We find that N_e grows with σ (Fig. 5F), suggesting that the

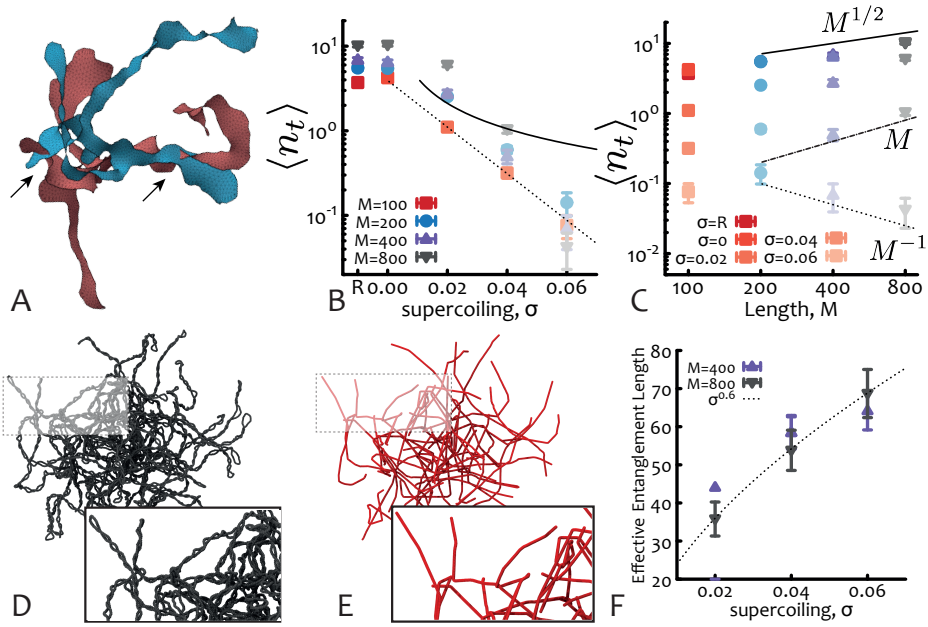

Figure 5. **Supercoiling Reduces Threadings and Entanglements.** **A** Snapshot of two threading plasmids (relaxed, $M = 800$) with minimal surfaces drawn and intersections highlighted by arrows. **B** Number of threadings per plasmid as a function of supercoiling (dashed=exponential, solid=$1/\sigma$). **C** Number of threadings per plasmid as a function of plasmid length (dashed=$1/M$, solid=$M^{1/2}$, dot-dashed=M). **D,E** Snapshots of the PPA analysis run on our system with plasmids $M = 800$ and $\sigma = 0.06$. **F** The effective entanglement length increases with supercoiling as $N_e \sim s^{0.6}$ for $M = 800$.

larger the supercoiling the less entangled the plasmids. For instance, we find that the effective linear backbone of the longest relaxed plasmids ($M = 400$) with $\sigma = 0.06$ is only about 3 entanglement lengths long. We argue that this unexpected supercoiling-driven reduction in entanglements is due to the fact that supercoiling increases the local concentration of intra-chain beads [64] in turn inflating the effective tube surrounding any one plasmid. Notice that for short plasmids the PPA method cannot identify entanglement length, confirming that these are very poorly entangled and hence only weakly affected by inter-chain entanglements (thus confirming our argument for the behaviour of R_g in Fig. 2).

Conclusions In this work we have simulated entangled solutions of DNA plasmids to study how supercoiling can be leveraged to tune the DNA dynamics orthogonally to other traditional methods, such as length or concentration. We have discovered that, contrarily to what typically assumed, the size of long plasmids increases with supercoiling when in entangled solutions. Surprisingly, we find that instead the mobility of the plasmids is enhanced by supercoiling. We discovered that this is due to severely asymmetric conformations which greatly reduce the number of threadings. In parallel, also generic entanglements are reduced as supercoiling increases the local concentration of intra-chain contacts thus effectively inflating the tube formed by neighbouring chains. We thus discovered that the unexpected enhanced diffusivity of entangled supercoiled DNA is due to a combination of reduced threading and entanglements.

We conjecture that highly supercoiled, longer plasmids in entangled solutions may display branched architectures, triggering the need of arm retraction or plectoneme diffusion/hopping relaxation mechanisms; in turn, this would entail a re-entrant slowing down of the plasmids diffusion. This non-monotonic dependence of DNA mobility on supercoiling would allow even richer control of the rheological properties.

Given our highly counter-intuitive results and the marked effect of supercoiling on plasmids microrhelogy we believe that our work will stimulate in vitro experiments using DNA plasmids extracted from bacteria and screened for desired levels of supercoiling. Albeit difficult, this is now nearly technically feasible [31]. Ultimately, understanding how DNA topology and supercoiling affect the dynamics and conformational properties of plasmids in *entangled* or *crowded* conditions may not only reveal novel pathways to achieve fine tuning of the rheology of biopolymer complex fluids but also shed light on fundamental biological processes.

MATERIALS AND METHODS

Molecular Dynamics

Each bead in our simulation is evolved through the Langevin equation $m_a \partial_{tt} \vec{r}_a = -\nabla U_a - \gamma_a \partial_t \vec{r}_a + \sqrt{2k_B T \gamma_a} \vec{\eta}_a(t)$, where m_a and γ_a are the mass and the friction coefficient of bead a, and $\vec{\eta}_a$ is its stochastic noise vector satisfying the fluctuation-dissipation theorem. U is the sum of the energy fields (see SI). The simulations

are performed in LAMMPS [34] with $m = \gamma = k_B = T = 1$ and using a velocity-Verlet algorithm with integration time step $\Delta t = 0.002\,\tau_B$, where $\tau_B = \gamma\sigma^2/k_BT$ is the Brownian time.

Branching Analysis

Following Refs. [61, 65], we compute the absolute writhe of a segment of a plasmid as $W(s) = (1/4\pi)\int_{s-l}^{s}\int_{s}^{s+l}|(\boldsymbol{r}_1-\boldsymbol{r}_2)\cdot(d\boldsymbol{r}_1\times d\boldsymbol{r}_2)/|\boldsymbol{r}_1-\boldsymbol{r}_2|^3|$ with window $l = 50$ beads. This calculation yields a function $W(s)$ whose maxima represent regions of high local writhe and can identify tips of plectonemes. In addition to being a local maximum, we require that $W(s) > 0.35$ to avoid false positives. See SI for more details.

Primitive Path Analysis

Following Ref. [63], we fix certain polymer segments in space, turn intra-chain repulsive interactions off and keep inter-chain interactions on. We then run simulations at low temperature 0.01 to find a ground state. The resulting chain conformations (primitive paths) are made of straight segments connected by sharp kinks due to entanglements. The entanglement length is then given by $N_e = r_{\rm ee}^2/(Mb_{pp}^2)$, where $r_{\rm ee}$ is the mean endpoint distance, M is the number of monomers between the fixed points and b_{pp} is the mean bond-length of the primitive path. We adapt the classical PPA for plasmids by fixing the tips of all detected plectonemes instead of the end points of linear chains (see SI).

Acknowledgements

The authors would like to acknowledge the networking support by the "European Topology Interdisciplinary Action" (EUTOPIA) CA17139. This project has received funding from the European Union's Horizon 2020 programme under grant agreement No. 731019 (EUSMI). DM acknowledges the computing time provided on the supercomputer JURECA at Jülich Supercomputing Centre and the Leverhulme Trust (ECF-2019-088). JS acknowledges the support from the Austrian Science Fund (FWF) through the Lise-Meitner Fellowship No. M 2470-N28. JS is grateful for the computational time at Vienna Scientific Cluster. Sample codes can be found at `git.ecdf.ed.ac.uk/dmichiel/supercoiledplasmids`.

[1] S. H. Um, J. B. Lee, N. Park, S. Y. Kwon, C. C. Umbach, and D. Luo, Nat. Mater. **5**, 797 (2006).
[2] P. W. K. Rothemund, Nature **440**, 297 (2006).
[3] N. C. Seeman and H. F. Sleiman, Nat. Rev. Mater. **3**, 1 (2017).
[4] C. Mao, W. Sun, and N. C. Seeman, Nature **386**, 137 (1997).
[5] C. E. Castro, F. Kilchherr, D. N. Kim, E. L. Shiao, T. Wauer, P. Wortmann, M. Bathe, and H. Dietz, Nat. Methods **8**, 221 (2011).
[6] M. E. Leunissen, R. Dreyfus, R. Sha, T. Wang, N. C. Seeman, D. J. Pine, and P. M. Chaikin, Soft Matter **5**, 2422 (2009).
[7] A. Bates and A. Maxwell, *DNA topology* (Oxford University Press, 2005).
[8] R. M. Robertson, S. Laib, and D. E. Smith, Proc. Natl. Acad. Sci. USA **103**, 7310 (2006).
[9] R. M. Robertson and D. E. Smith, Proc. Natl. Acad. Sci. USA **104**, 4824 (2007).
[10] R. E. Teixeira, A. K. Dambal, D. H. Richter, E. S. G. Shaqfeh, and S. Chu, Macromolecules **40**, 3514 (2007).
[11] R. Fitzpatrick, D. Michieletto, K. R. Peddireddy, C. Hauer, C. Kyrillos, B. J. Gurmessa, and R. M. Robertson-anderson, Phys. Rev. Lett. **121**, 257801 (2018).
[12] D. Michieletto, R. Fitzpatrick, and R. M. Robertson-Anderson, Soft Matter , 6703 (2019).
[13] D. Racko, F. Benedetti, D. Goundaroulis, and A. Stasiak, Polymers (Basel). **10**, 1 (2018).
[14] F. Benedetti, J. Dorier, Y. Burnier, and A. Stasiak, Nucleic Acids Res. **42**, 2848 (2014).
[15] N. Gilbert and J. Allan, Curr. Opin. Genet. Dev. **25**, 15 (2014).
[16] C. Naughton, N. Avlonitis, S. Corless, J. G. Prendergast, I. K. Mati, P. P. Eijk, S. L. Cockroft, M. Bradley, B. Ylstra, and N. Gilbert, Nat. Struct. Mol. Biol. **20**, 387 (2013).
[17] R. N. Irobalieva, J. M. Fogg, D. J. C. Jr, T. Sutthibutpong, M. Chen, A. K. Barker, S. J. Ludtke, S. A. Harris, M. F. Schmid, W. Chiu, and L. Zechiedrich, Nat. Commun. **6**, 1 (2015).
[18] Y. A. G. Fosado, D. Michieletto, and D. Marenduzzo, Phys. Rev. Lett. **119**, 1 (2017), arXiv:1703.08367.
[19] A. Vologodskii, Phys. Life Rev. **18**, 118 (2016).
[20] T. Sutthibutpong, C. Matek, C. Benham, G. G. Slade, A. Noy, C. Laughton, J. P. Doye, A. A. Louis, and S. A. Harris, Nucleic Acids Res. **44**, 9121 (2016).
[21] Y. Ding, C. Manzo, G. Fulcrand, F. Leng, D. Dunlap, and L. Finzi, Proc. Natl. Acad. Sci. USA **111**, 15402 (2014).
[22] S. Laib, R. M. Robertson, and D. E. Smith, Macromolecules **39**, 4115 (2006).
[23] X. Zhu, B. Kundukad, and J. R. Van Der Maarel, J. Chem. Phys. **129**, 1 (2008).
[24] A. Rosa, J. Smrek, M. S. Turner, and D. Michieletto, ACS Macro Letters **9**, 743 (2020), arXiv:arXiv:1908.06638v2.
[25] B. W. Soh, A. R. Klotz, R. M. Robertson-Anderson, and P. S. Doyle, Phys. Rev. Lett. **123**, 048002 (2019).
[26] B. A. Krajina, A. Zhu, S. C. Heilshorn, and A. J. Spakowitz, Phys. Rev. Lett. **121**, 148001 (2018).
[27] C. A. Brackley, A. N. Morozov, and D. Marenduzzo, J. Chem. Phys. **140**, 135103 (2014).
[28] B. A. Krajina and A. J. Spakowitz, Biophys J. **111**, 1339 (2016).
[29] J. Cebrián, M. J. Kadomatsu-Hermosa, A. Castán, V. Martínez, C. Parra, M. J. Fernández-Nestosa,

C. Schaerer, M.-L. Martínez-Robles, P. Hernández, D. B. Krimer, A. Stasiak, and J. B. Schvartzman, Nucleic Acids Res. **3112**, 1 (2014).
[30] M. Doi and S. Edwards, *The theory of polymer dynamics* (Oxford University Press, 1988).
[31] K. R. Peddireddy, M. Lee, Y. Zhou, S. Adalbert, S. Anderson, C. M. Schroeder, and R. M. Robertson-Anderson, Soft Matter **16**, 152 (2019).
[32] J. F. Marko and E. D. Siggia, Macromolecules **27**, 981 (1994).
[33] K. Kremer and G. S. Grest, J. Chem. Phys. **92**, 5057 (1990).
[34] S. Plimpton, J. Comp. Phys. **117**, 1 (1995).
[35] M. R. Dennis and J. H. Hannay, , 3245 (2005), arXiv:0503012 [math-ph].
[36] F. B. Fuller, Proc. Natl. Acad. Sci. USA **68**, 815 (1971).
[37] J. H. White, K. C. Millett, and N. Cozzarelli, J. Mol. Biol. **197**, 585 (1987).
[38] J. D. Halverson, W. B. Lee, G. S. Grest, A. Y. Grosberg, and K. Kremer, J. Chem. Phys. **134**, 204904 (2011), arXiv:arXiv:1104.5653v1.
[39] R. R. Sinden and D. E. Pettijohn, Proceedings of the National Academy of Sciences of the United States of America **78**, 224 (1981).
[40] F. Wu, A. Japaridze, X. Zheng, J. Wiktor, J. W. Kerssemakers, and C. Dekker, Nature Communications **10**, 1 (2019).
[41] N. Gilbert and J. Allan, Current Opinion in Genetics and Development **25**, 15 (2014).
[42] F. Benedetti, D. Racko, J. Dorier, Y. Burnier, and A. Stasiak, Nucleic Acids Res. **45**, 9850 (2017).
[43] K. Ott, L. Martini, J. Lipfert, and U. Gerland, Biophysical Journal **118**, 1690 (2020).
[44] M. Bernabei, P. Bacova, A. J. Moreno, A. Narros, and C. N. Likos, Soft Matter **9**, 1287 (2013).
[45] J. D. Halverson, W. B. Lee, G. S. Grest, A. Y. Grosberg, and K. Kremer, J. Chem. Phys. **134**, 204905 (2011).
[46] A. Rosa and R. Everaers, Phys. Rev. Lett. **112**, 118302 (2014), arXiv:arXiv:1310.7641v1.
[47] M. Z. Slimani, P. Bacova, M. Bernabei, A. Narros, C. N. Likos, and A. J. Moreno, ACS Macro Letters **3**, 611 (2014), arXiv:1309.1061.
[48] D. Michieletto and M. S. Turner, Proc. Natl. Acad. Sci. USA **113**, 5195 (2016), arXiv:arXiv:1510.05625v1.
[49] D. Michieletto, N. Nahali, and A. Rosa, Phys. Rev. Lett. **119**, 197801 (2017), arXiv:1703.09688.
[50] J. Smrek and A. Y. Grosberg, ACS Macro Lett. **5**, 750 (2016).
[51] J. Smrek, I. Chubak, C. N. Likos, and K. Kremer, Nature Communications **11**, 1 (2020).
[52] E. J. Rawdon, J. C. Kern, M. Piatek, P. Plunkett, A. Stasiak, and K. C. Millett, Macromolecules **41**, 8281 (2008).
[53] F. Benedetti, A. Japaridze, J. Dorier, D. Racko, R. Kwapich, Y. Burnier, G. Dietler, and A. Stasiak, Nucleic Acids Res. **43**, 2390 (2015).
[54] A. Rosa, E. Orlandini, and L. Tubiana, Macromolecules **44**, 8668 (2011).
[55] M. Lang, Macromolecules **46**, 1158 (2013).
[56] L. R. Gómez, N. A. García, and T. Pöschel, Proceedings of the National Academy of Sciences of the United States of America **117**, 3382 (2020).
[57] J. Smrek, K. Kremer, and A. Rosa, ACS Macro Lett. **8**, 155 (2019).
[58] R. D. Schram, A. Rosa, and R. Everaers, Soft Matter **15**, 2418 (2019).
[59] Y. Doi, A. Takano, Y. Takahashi, and Y. Matsushita, Macromolecules **48**, 8667 (2015).
[60] R. Everaers, A. Y. Grosberg, M. Rubinstein, and A. Rosa, Soft Matter (2017), 10.1039/C6SM02756C.
[61] D. Michieletto, Soft Matter **12**, 9485 (2016).
[62] A. V. Vologodskii, S. D. Levene, K. V. Klenin, M. Frank-Kamenetskii, and N. R. Cozzarelli, Journal of Molecular Biology **227**, 1224 (1992).
[63] R. Everaers, S. K. Sukumaran, G. S. Grest, C. Svaneborg, A. Sivasubramanian, and K. Kremer, Science (80-.). **303**, 823 (2004).
[64] A. V. Vologodskii and N. R. Cozzarelli, J. Mol. Biol. **227**, 1224 (1992).
[65] K. Klenin and J. Langowski, Biopolymers **54**, 307 (2000).

Supercoiling Enhances DNA Mobility by Reducing Threadings and Entanglements: Supplementary Information

Jan Smrek[1] and Davide Michieletto[2,3]

[1] *Faculty of Physics, University of Vienna, Boltzmanngasse 5, A-1090 Vienna, Austria*
[2] *School of Physics and Astronomy, University of Edinburgh, Peter Guthrie Tait Road, Edinburgh, EH9 3FD, UK*
[3] *MRC Human Genetics Unit, Institute of Genetics and Molecular Medicine, University of Edinburgh, Edinburgh EH4 2XU, UK*

MD simulations

DNA is represented as a twistable elastic chain (as detailed in Ref. [1]) whereby the backbone is made of beads each decorated by three patches (please refer to Fig. 1 in the main text).The backbone beads interact via a purely repulsive Lennard-Jones potential as

$$U_{\rm LJ}(r) = \begin{cases} 4\epsilon\left[\left(\frac{\sigma_b}{r}\right)^{12} - \left(\frac{\sigma_b}{r}\right)^{6} + \frac{1}{4}\right] & r \le r_c \\ 0 & r > r_c \end{cases}, \quad (1)$$

where r denotes the separation between the bead centers. The cutoff distance $r_c = 2^{1/6}\sigma$ is chosen so that only the repulsive part of the Lennard-Jones is used. The energy scale is set by $\epsilon = \kappa_B T$ and the length scale by σ_b, both of which are set to unity in our simulations. Consistent with that, in this work all quantities are reported in reduced LJ units. The size of each bead in real units should be considered as the thickness of DNA, i.e. $\sigma = 2.5$ nm or $= 2.5/0.34 \simeq 7.35$ bp per bead. The patches have no steric interactions.

Nearest-neighbour beads along the backbone are connected by finitely extensible nonlinear elastic (FENE) springs as

$$U_{\rm FENE}(r) = \begin{cases} -0.5kR_0^2 \ln\left(1-(r/R_0)^2\right) & r \le R_0 \\ \infty & r > R_0 \end{cases}, \quad (2)$$

where $k = 40\epsilon/\sigma_b^2$ is the spring constant and $R_0 = 1.6\sigma_b$ is the maximum extension of the elastic FENE bond.

To model DNA's stiffness (150 bp or 50 nm) we introduce an additional bending energy penalty between consecutive triplets of neighbouring beads along the backbone in order to control polymer stiffness:

$$U_{\rm bend}(\theta) = k_\theta\left(1-\cos\theta\right) . \quad (3)$$

Here, θ is the angle formed between adjacent bonds, i.e. $\boldsymbol{t}_i \cdot \boldsymbol{t}_{i+1}/|\boldsymbol{t}_i||\boldsymbol{t}_{i+1}|$ with $\boldsymbol{t}_i$ the tangent at i, and $k_\theta = 20\kappa_B T$ is the bending constant. With this choice $l_p = 20\sigma_b \simeq 50$ nm is the persistence length.

To model the torsional stiffness, two dihedral CHARMM springs constrain the relative rotation of consecutive beads, ψ, at a user-defined value (ψ_0). The torsional angle ψ is determined as the angle between planes defined by the triplets bead-bead-patch running along the DNA backbone. The potential is

$$U_{\rm torsion}(\psi) = k_\psi\left[1+\cos\left(n\psi - d\right)\right] \quad (4)$$

where $k_\psi = 50k_BT$, $n = 1$ and $d = \psi_0$. The angle ψ_0 directly determines the thermodynamically preferred pitch of the twisted ribbon as $p = 2\pi/\psi_0$ and, in turn, this determines the preferred linking number as $Lk = N/p$, where N is the number of beads in the plasmid. In this model, $Lk_0 = 0$ and $\sigma \equiv \Delta Lk/N = Lk/N = 1/p$, which is set by initialising the patchy-polymer as a flat ribbon and by subsequently imposing the angle ψ_0 in order to achieve the wanted σ (which may be zero, if $\psi_0 = 0$ or $p = \infty$).

Finally, to maintain consecutive beads parallel to the backbone, we constrain the angle between the triplets bead-bead-patch to $\gamma = \pi/2$ so that the frames of reference formed by the triplets are aligned to each other. This potential is written as

$$U_{\rm align} = k_\gamma\left(1-\cos\gamma\right) . \quad (5)$$

with $k_\gamma = 200k_BT$.

The simulations are performed at fixed monomer density $\rho\sigma_b^3 = 0.08$ (equivalent to about 39 mg/ml of DNA), where $\sigma_b = 2.5$ nm$= 7.35bp$ is the typical size of a bead, and by evolving the equation of motion for the beads coupled to a heath bath which provides noise and friction. The equation of motion is thus given by

$$m_a\partial_{tt}\vec{r}_a = -\nabla U_a - \gamma_a\partial_t\vec{r}_a + \sqrt{2k_BT\gamma_a}\vec{\eta}_a(t) , \quad (6)$$

where m_a and γ_a are the mass and the friction coefficient of bead a, and $\vec{\eta}_a$ is its stochastic noise vector satisfying the fluctuation-dissipation theorem. U is the sum of the energy fields described above. The simulations are performed in LAMMPS [2] with $m = \gamma = k_B = T = 1$ and using a velocity-Verlet algorithm with integration time step $\Delta t = 0.002\,\tau_B$, where $\tau_B = \gamma\sigma^2/k_BT$ is the Brownian time. See also Table I for more details on the systems and Git repository `https://git.ecdf.ed.ac.uk/dmichiel/supercoiledplasmids/` for sample codes to reproduce these simulations.

Equilibration

Since we are simulating circular polymers (which are also torsionally constrained) we cannot use bridge algorithms to relax the chains, instead we typically perform equilibrium simulations until key observables of the systems have reached a steady state. We monitor both, the gyration radius and the displacement of the molecules, and deem the system equilibrated when each molecule has travelled at least its own size in equilibrium. After that, we perform the production run.

In total, we have performed 20 sets of simulations, 5 supercoiling levels (relaxed, $\sigma = 0, 0.02, 0.04, 0.06$) per 4 choices of plasmid length ($M = 100, 200, 400, 800$). The number of plasmids in each system is $N = 160, 80, 40, 40$ meaning that there are 64'000 atoms per each system (and 128'000 for the one with $M = 800$, recall that each DNA bead is made by 4 atoms, one backbone and 3 patches). Thanks to the European Soft Matter Infrastructure we were able to run most of these simulations on the supercomputer JURECA and some on Vienna Scientific Cluster, consuming together about 2M CPU-h.

Detections of Tips and Plectonemes

The detection of tips and plectonomes in plasmids is done following the method described in Ref. [3]. Briefly, we compute the absolute writhe of a segment s of a plasmid as

$$W(s) = \frac{1}{4\pi} \int_{s-l}^{s} \int_{s}^{s+l} \left| \frac{(\boldsymbol{r}_1 - \boldsymbol{r}_2) \cdot (d\boldsymbol{r}_1 \times d\boldsymbol{r}_2)}{|\boldsymbol{r}_1 - \boldsymbol{r}_2|^3} \right| \quad (7)$$

where l is set to 50 beads as about 2 persistence lengths (which was shown to be a reasonable window size in Ref. [3]. This calculation yields a function $W(s)$ whose maxima represent regions of high local writhe and can identify tips of plectonemes. In addition to being a local maximum, we require that $W(s) > 0.35$ to avoid false positives. We checked that while the number of detected tips depends slightly on the threshold value and the tip length l, the primitive path analysis is robust with respect to usage of a more stringent choice of threshold 0.5 and $l = 40$. In Fig. S5 below we plot the average number of tips $\langle n_{\text{tips}} \rangle$ per plasmid. One can readily notice that for low supercoiling the dispersion is quite large, indicating that the plasmids assume loose conformations with several tip-like segments along the contour. On the contrary, for large supercoiling one can notice that they become narrowly dispersed around $\langle n_{\text{tips}} \rangle = 2$ indicating that the plasmids assume linear-like (rather than branched) conformations. Additionally, it is interesting to appreciate that $\langle n_{\text{tips}} \rangle$ is very close to zero for short $M = 100$ plasmids with $\sigma = 0$ once again indicating locked swollen conformations, as shown in the main text.

Primitive Path Analysis

The primitive path analysis for linear polymers [4] is based on fixing the chains' endpoints in space, switching off the intra-chain repulsive interaction, while keeping the inter-chain and running the simulation at low temperature 0.01 to find a ground state. The resulting chain conformations (primitive paths) are composed of straight segments connected by sharp kinks due to inter-chain entanglements. The entanglement length is then given by $N_e = r_{\text{ee}}^2/(M b_{pp}^2)$, where r_{ee} is the mean endpoint distance, M is the number of monomers between the fixed points and b_{pp} is the mean bond-length of the primitive path. We adapt the PPA for plasmids by fixing the tips of all detected plectonemes and then by following the same protocol as for linear chains.

For example, in the most common case of two tips per plasmid, both segments between the tips forming the plasmid contribute to N_e and are considered as independent for that purpose. In some cases the branch-detecting method fails to localize all tips and detects only one tip. In that case, we fix also the monomer $M/2$ contour-wise apart from a detected tip. In most cases this coincides with a tip detected with a lower detection threshold. If no tips are detected in one or more plasmids, the snapshot is excluded from the calculation. This does not happen for plasmids with $\sigma = 0.06$, happens rarely (in about 5% of cases) in for $\sigma = 0.04$ and frequently (about 60%) for the lower supercoiling $\sigma = 0.02$. This is natural as the less supercoiled plasmids have looser conformations where the branches are less clearly definable. We analyze about 50 to 100 snapshots each separated by at least $2.10^5 \tau_{\text{B}}$. We check the method is robust with respect to the choice of the threshold value $0.35 - 0.5$ and the detection length $40 - 50$ beads, and gives within errorbars the same value of N_e. In contrast to equilibrium rings [5], we find our results do not strongly depend on the plasmid length, which gives the credence to the method and highlights the role of linear-like entanglement present for supercoiled plasmids. The small deviations within the errorbars are attributed to the finite size of the examined plasmids. For that reason we used only the longer systems with $M = 800$ and $M = 400$ to have at least $3 - 5$ statistically independent entanglement segments.

SUPPLEMENTARY TABLE

SUPPLEMENTARY FIGURES

[1] C. A. Brackley, A. N. Morozov, and D. Marenduzzo, J. Chem. Phys. **140**, 135103 (2014).

[2] S. Plimpton, J. Comp. Phys. **117**, 1 (1995).

[3] D. Michieletto, Soft Matter **12**, 9485 (2016).

[4] R. Everaers, S. K. Sukumaran, G. S. Grest, C. Svaneborg, A. Sivasubramanian, and K. Kremer, Science (80-.). **303**, 823 (2004).

[5] J. D. Halverson, W. B. Lee, G. S. Grest, A. Y. Grosberg, and K. Kremer, J. Chem. Phys. **134**, 204905 (2011).

[6] E. J. Rawdon, J. C. Kern, M. Piatek, P. Plunkett, A. Stasiak, and K. C. Millett, Macromolecules **41**, 8281 (2008).

[7] R. D. Schram, A. Rosa, and R. Everaers, Soft Matter **15**, 2418 (2019).

M	N	σ	$\langle R_{\rm g}^2\rangle/\sigma_b^2$	$\langle R_{\rm m}^2\rangle/\sigma_b^2$	Σ/σ_b^2	$D.10^4\tau_{\rm B}\sigma_b^2$	$n_{\rm tips}$	$t_{\rm total}/10^6\tau_{\rm B}$	$t_{\rm CPU}/10^4$hrs	
100	160	R	154 (2)	357(10)	420 (125)		105 (1)	0.55 (0.58)	0.52	0.5
100	160	0	177 (1)	496 (7)	526 (83)		75 (4)	0.05 (0.08)	0.40	0.4
100	160	0.02	121 (1)	123 (3)	206 (28)		127 (5)	1.93 (0.12)	0.40	0.4
100	160	0.04	122 (1)	57 (2)	124 (12)		179 (5)	2.006 (0.007)	0.40	0.4
100	160	0.06	123 (1)	29 (1)	87 (8)		242 (2)	2.004 (0.005)	0.40	0.4
200	80	R	369 (9)	391 (20)	693 (244)		14 (2)	0.88 (0.62)	2.43	2.5
200	80	0	390 (16)	457 (31)	724 (238)		18 (2)	0.72 (0.53)	1.01	1
200	80	0.02	362 (10)	208 (10)	457 (70)		15 (2)	1.48 (0.52)	1.01	1
200	80	0.04	387 (10)	84 (4)	260 (24)		37 (2)	2.02 (0.05)	1.01	1
200	80	0.06	395 (8)	41 (2)	177 (12)		62 (2)	2.02 (0.02)	0.96	1
400	40	R	739 (37)	612 (35)	1385 (358)		1.8^*	1.30 (0.91)	8.77	8.9
400	40	0	818 (34)	650 (37)	1398 (385)		1.6^*	1.03 (0.75)	7.95	8.1
400	40	0.02	870 (46)	322 (19)	955 (146)		2.2^*	1.59 (0.87)	7.91	8.0
400	40	0.04	1043 (45)	118 (8)	526 (44)		6.98 (0.01)	2.13 (0.32)	7.45	7.5
400	40	0.06	1114 (53)	53 (4)	349 (20)		15.80 (0.01)	2.04 (0.05)	7.28	7.3
800	40	R	1245 (32)	865 (55)	2623 (484)		0.4^*	2.41 (1.57)	12.3	25
800	40	0	1262 (57)	807 (47)	2680 (495)		0.6^*	1.94 (1.53)	15.8	32
800	40	0.02	1480 (61)	502 (31)	2042 (264)		0.5^*	2.81 (1.77)	15.8	32
800	40	0.04	1966 (76)	167 (11)	1063 (79)		1.34 (0.01)	2.78 (1.00)	16.2	33
800	40	0.06	2524 (96)	67 (5)	684 (30)		2.89 (0.01)	2.16 (0.19)	13.9	28

Table I. **System details**. Number in parenthesis correspond to the standard deviation. For the diffusion coefficient they represent the error on the fit on the last digit. Values of diffusion coefficient marked by * are upper estimates as the systems were not fully diffusive. Total simulation time 2M CPU-hours.

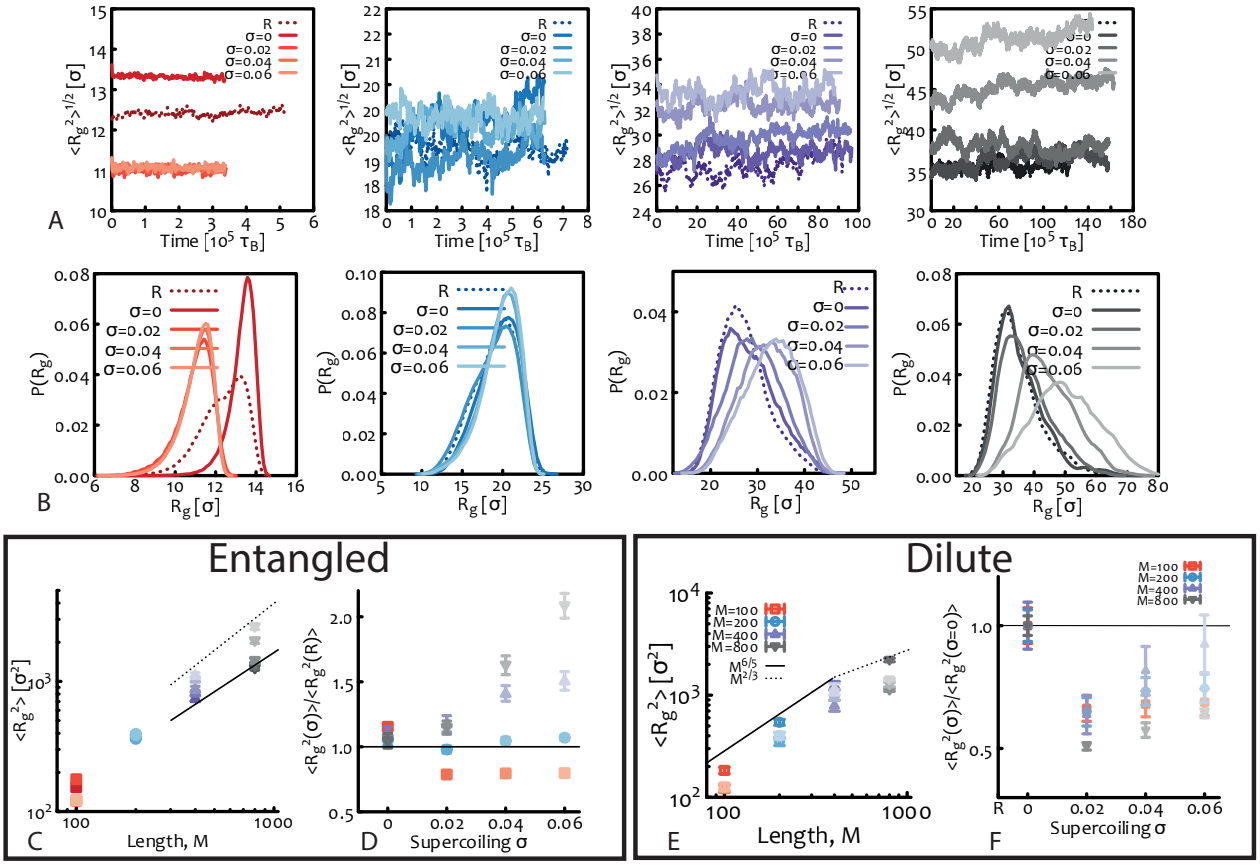

Figure 1. **A.** Time trace of the ensemble-averaged radius of gyration $\langle R_g^2 \rangle^{1/2}$ for $M = 100, 200, 400, 800$ (from left to right). **B.** Distributions of the radius of gyration. **C-D.** Scaling of the square radius of gyration as a function of length and supercoiling in **entangled** solutions. **E-F.** Scaling of the square radius of gyration as a function of length and supercoiling in **dilute** solutions, here we consider 10 times lower monomer density i.e. $\rho\sigma_b^3 = NM/L^3 = 0.008$.

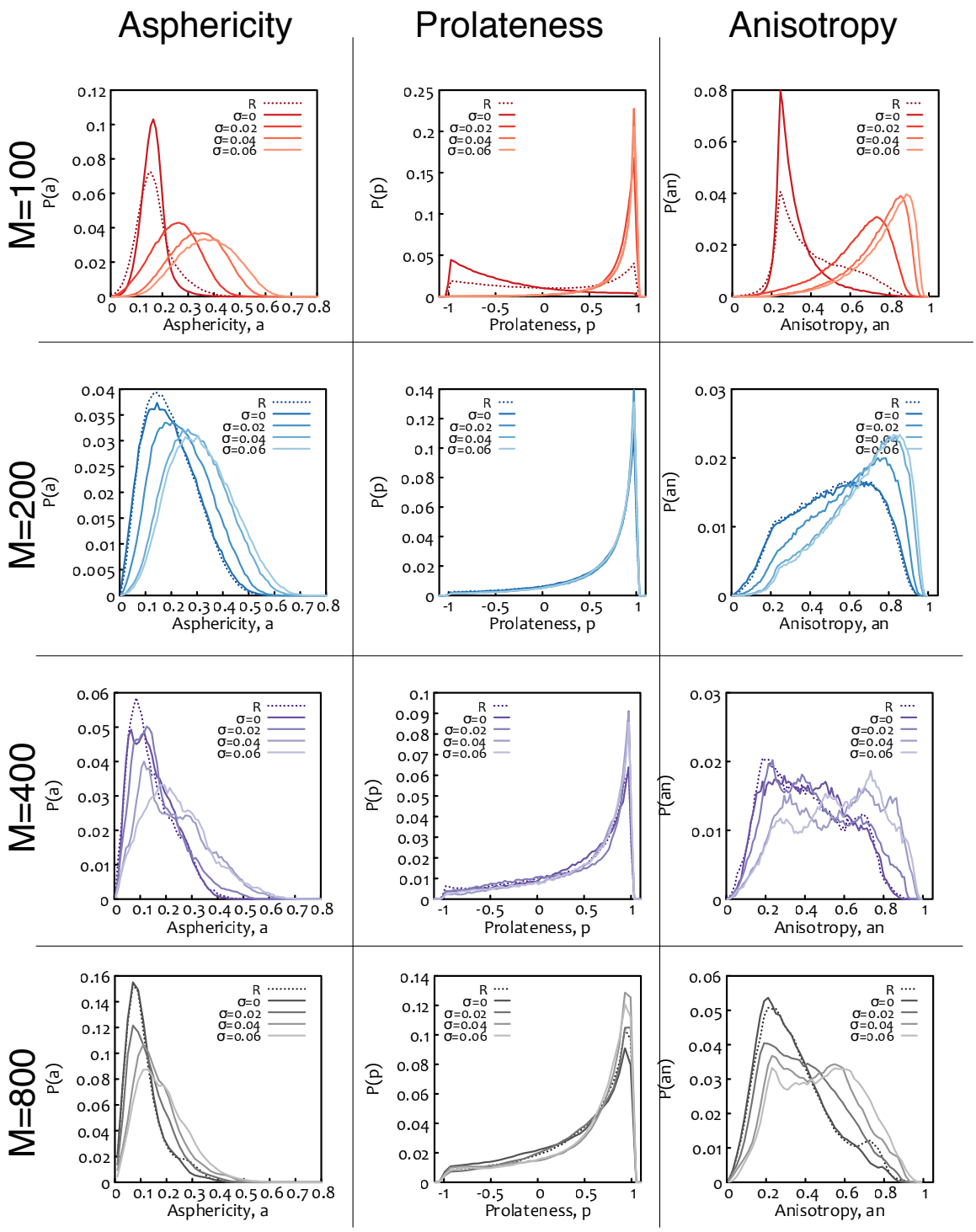

Figure 2. Summary of shape descriptors. Asphericity $A = ((a-b)^2 + (a-c)^2 + (b-c)^2)/2R_g^4$, anisotropy $an = 3(a^2+b^2+c^2)/(2R_g^4) - 1/2$ and prolateness $p = (2a-b-c)(2b-a-c)(2c-a-b)/2(a^2+b^2+c^2-ab-ac-bc)^{3/2}$ [6].

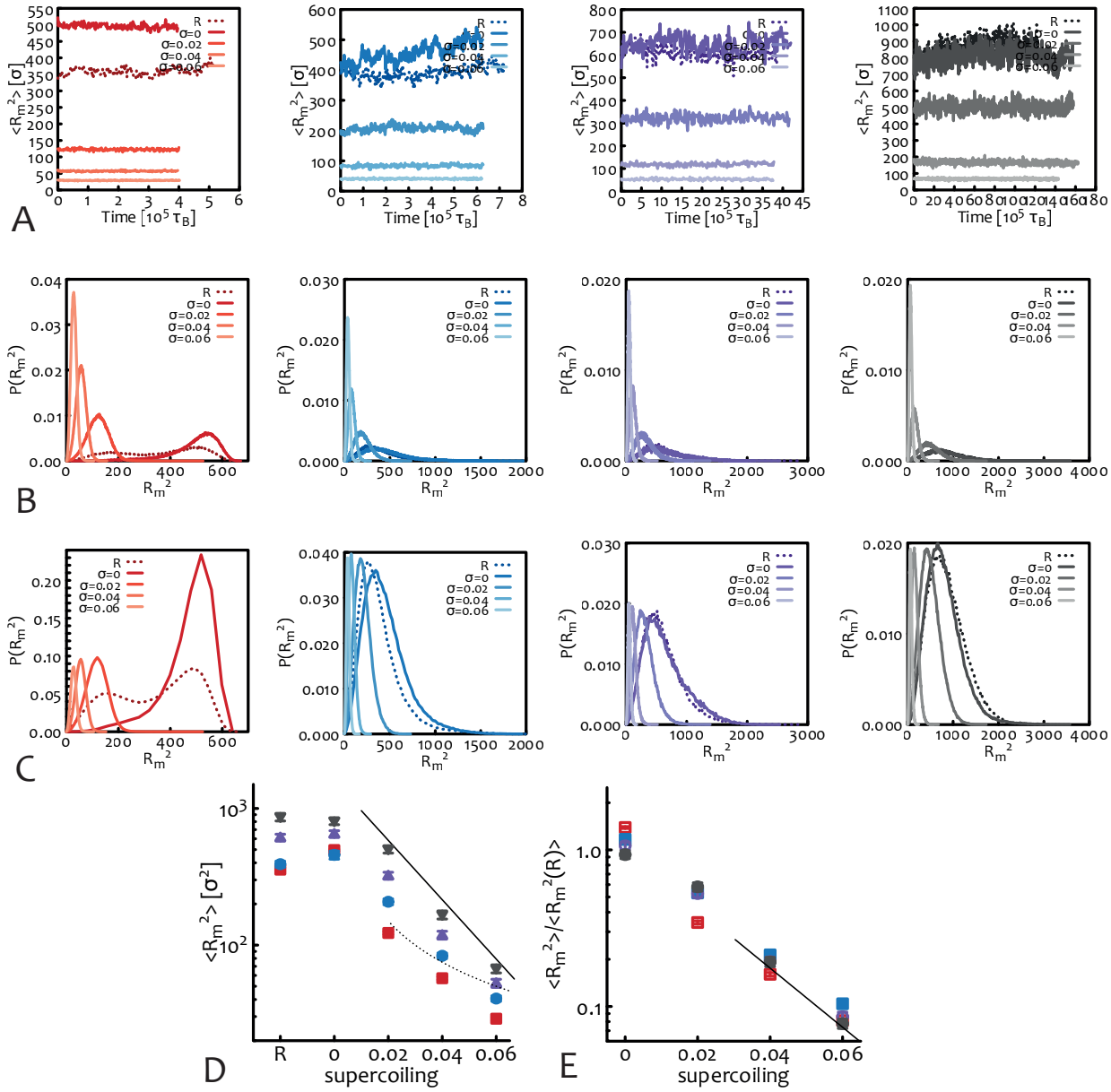

Figure 3. So-called magnetic radius R_m is computed from magnetic moment $\boldsymbol{A} = \sum_{i=1}^{M} \boldsymbol{r}_i \times (\boldsymbol{r}_{i+1} - \boldsymbol{r}_i)$ [7], as $R_m^2 = 0.5|\boldsymbol{A}|$, which quantifies the effective area subtended by the magnetic moment. From the definition of $\boldsymbol{A}$, one can notice that the moment is maximum for a perfectly circle and identically 0 on a perfectly double folded curve (which does not allow contours of other chains to pass through it). **A.** Time trace of the ensemble-averaged square magnetic radius R_m^2. **B.** Distributions of the square magnetic radius for fixed bin width ($\Delta R_m^2 = 1$). The distributions of R_m^2 again display a bistable state for short plasmids in an open and double-folded states which are respectively stabilised by setting $\sigma = 0$ and $\sigma > 0$. Aside from the special case of short plasmids, increasing the supercoiling typically reduces the average magnetic radius for any $\sigma > 0$ **C.** Same as B, this time plotted for a fixed total number of bins (=1000) and different bin width to best compare the distributions (notice the bimodal distribution for relaxed plasmids $M = 100$). From left to right $M = 100, 200, 400, 800$. **D.** Scaling of the square magnetic radius with supercoiling. **E.** Same as D, normalised by the square magnetic radius of the relaxed plasmids. Solid lines show an exponential decay, whereas dashed line a power law $1/\sigma$. Notice that the scaling of R_m^2 with sigma is more compatible with an exponential decay than the power law. Instead the minimal surface (see main text) scales closely to $1/\sigma$.

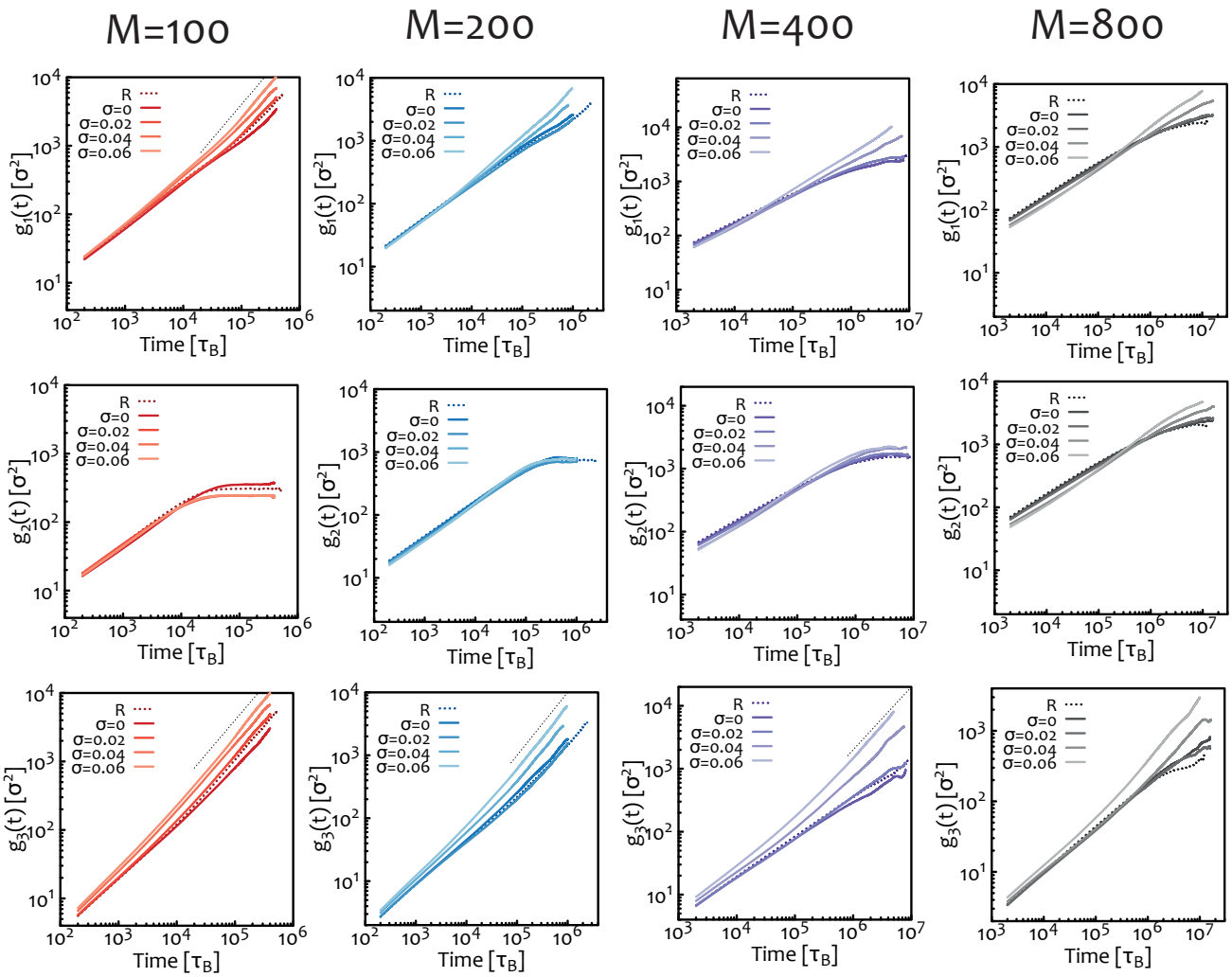

Figure 4. Plots of TAMSD, from top to bottom g_1, g_2, g_3 represent time and ensemble mean squared average displacement of the monomers (g_1), monomers with respect to the center of mass of each plasmid (g_2) and the center of mass of each ring with respect to the global center of mass (g_3).

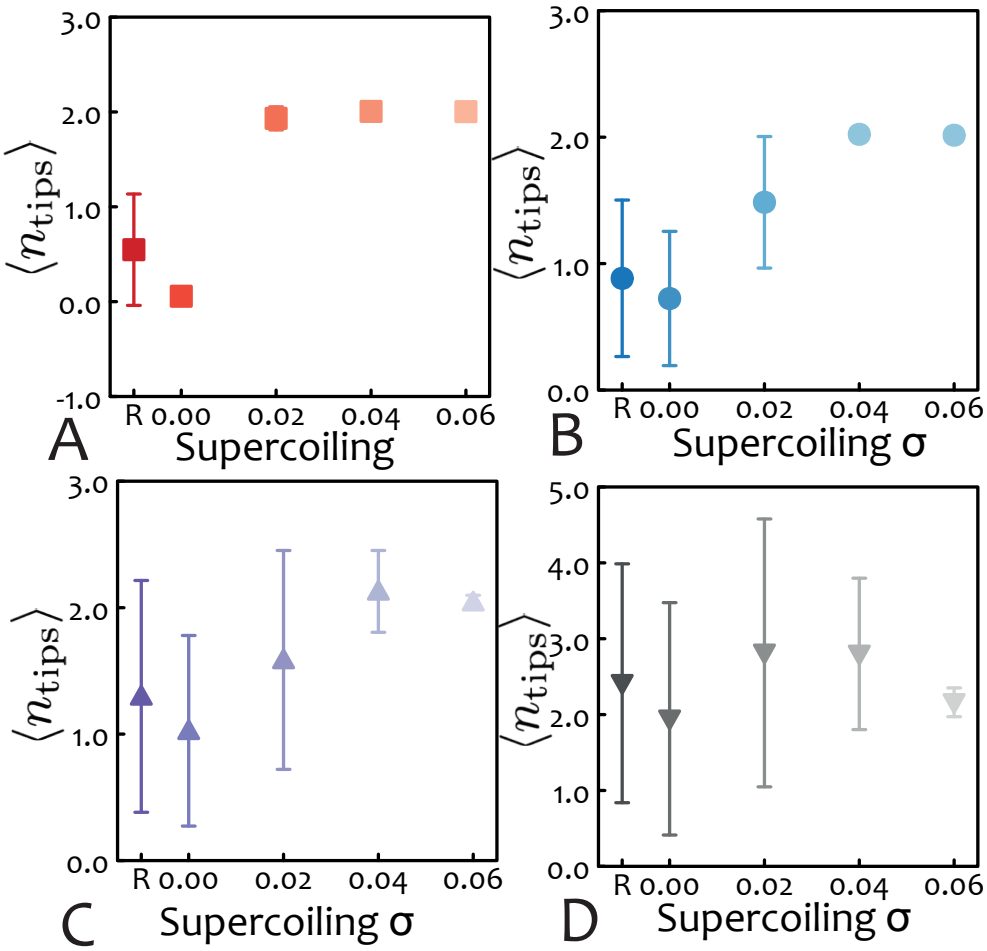

Figure 5. Plots of average number of tips for the different systems as a function of supercoiling. A. $M = 100$ B. $M = 200$ C. $M = 400$ D. $M = 800$.